Convolution Based Techniques for Computing Self Attraction and Loading in MOM6

Anthony Chen[1,6], He Wang[2,3,4], Brian K. Arbic[2,5], and Robert Krasny[1]

[1]Department of Mathematics, University of Michigan, Ann Arbor, MI, USA
[2]Department of Earth and Environmental Sciences, University of Michigan, Ann Arbor, MI, USA
[3]UCAR, Boulder, CO, USA
[4]NOAA-GFDL, Princeton, NJ, USA
[5]Research School of Earth Sciences, Australian National University, Canberra, ACT, Australia
[6]Department of Mathematics, National University of Singapore, Singapore

Correspondence: Anthony Chen (cygnari@umich.edu)

Abstract. Self Attraction and Loading (SAL), which accounts for the deformation of the solid Earth under the load of the ocean tide and the self-gravitation of the so-deformed Earth as well as of the ocean tides themselves, is an important effect to include in numerical models of the ocean tides. Computing the SAL potential and its gradient is a challenging problem that is often accomplished using the spherical harmonics transform (SHT), but that approach has drawbacks which limit its accuracy. This work employs an alternative approach based on computing the spherical convolution integral, which utilizes an approximate SAL Green's function and is accelerated by the recently developed Cubed Sphere Fast Multipole Method (CSFMM). The convolution technique is implemented in the Modular Ocean Model, version 6, where it provides more accurate tides than those obtained with the SHT when measured against tidal datasets based on satellite altimetry. Previous investigators have cited Gibbs phenomenon as a possible source of error in SHT calculations, but our application of Cesàro summation to the SHT failed to reduce the error, which suggests that other errors are also significant, such as aliasing error due to finite grid resolution, and finite difference errors in computing the gradient of the SAL potential. The convolution approach has different sources of error including errors in the approximate SAL Green's function, quadrature error in computing the convolution integral, and interpolation error from the CSFMM. In addition to comparing the accuracy of the two approaches, we also present the runtime for parallel calculations using up to 1024 MPI ranks.

1 Introduction

Tides are an important component of the Earth system. In many open-ocean and coastal regions, tides dominate sea level and/or current variability. Tides are also implicated as a major element in the ocean mixing cycle, which contributes significantly to the background oceanic stratification in both the coastal and open ocean (Simpson and Hunter, 1974; Munk and Wunsch, 1998). Tides are a result of astronomical gravitational forcing, and this tidal forcing drives periodic changes in the sea surface height (SSH) and the currents. Hence an improved understanding of tidal dynamics is necessary for developing improved models.

Historically, tides were independently modeled from the rest of the ocean, primarily in barotropic tide models, which improved with increased computing power and data assimilation from satellite altimetry (Egbert et al., 1994; Le Provost et al., 1994; Parke and Hendershott, 1980; Ray, 1993; Schwiderski, 1979; Shum et al., 1997; Stammer et al., 2014). The first studies of tides in a baroclinic model were performed in regional configurations (Cummins and Oey, 1997; Kang et al., 2002; Merrifield et al., 2001). In the past two decades, as computers have improved, tides have been explicitly incorporated into ocean general circulation models (Arbic, 2022; Arbic et al., 2010; Müller et al., 2010; Schiller and Fiedler, 2007; Thomas et al., 2001; Rocha et al., 2016; Waterhouse et al., 2014). Running such models with combined tidal and atmospheric forcing at high spatial resolution enables investigation of the interactions of barotropic and internal tides with oceanic phenomena across a wide range of scales, including mesoscale eddies, and other components of the Earth system including the cryosphere.

An important effect to capture when modeling the tides is Self Attraction and Loading (SAL). This encompasses the physical effects of the self gravitation of the oceanic tidal elevations, the elastic response of the Earth's crust to the loading of the ocean tide, and resulting changes in the Earth's gravitational potential due to the self gravitation of the deformed solid Earth (Hendershott, 1972). SAL has a large effect on tides, changing their amplitude by up to 20% and impacting their phase significantly as well (Gordeev et al., 1977). A simple computationally efficient approach to computing SAL uses the so-called scalar approximation (Accad and Pekeris, 1978), in which the SAL forcing term is approximated as a constant multiplied by the tidal elevation.

The scalar approximation however is less accurate than a treatment using spherical harmonics, which properly account for the response of the ocean and solid Earth to harmonics of different scales (Ray, 1998). Including the spherical harmonics SAL in tide models often took an iterative approach using offline computations (Arbic et al., 2004; Egbert et al., 2004), where the SAL was calculated outside of the model run. Early attempts to use the spherical harmonics SAL inline, as the model is running, found it to be too computationally expensive (Stepanov and Hughes, 2004). This is because SAL requires global communication, in contrast to other terms in the momentum equations of numerical ocean models. More recent modeling using an inline spherical harmonics SAL has been aided by improvements in computational power (Barton et al., 2022; Brus et al., 2023; Wang et al., 2024), yet this approach still encounters limitations on accuracy around coastlines (more below), and the fact that spherical harmonics, being global quantities, cannot easily be used in regional models.

Another approach to computing SAL, often used in the geodesy community, is based on convolution of the sea surface height with a Green's function (Farrell, 1972; Schrama, 2005; Agnew, 2012; Martens et al., 2019). This approach has been explored in post-processing contexts, but has never been incorporated into an ocean model due to the expense of computing the convolution integral over the sphere representing the Earth surface. Here we employ the recently developed Cubed Sphere Fast Multipole Method (CSFMM) to reduce the cost of computing the integral and enable inline SAL: calculations (Chen and Krasny, 2025). The convolution SAL is implemented in the Modular Ocean Model, version 6, and the results show that it provides more accurate tides than those obtained with the spherical harmonics approach.

The paper is organized as follows. Section 2 presents the governing equations, describes the various methods for computing SAL, introduces our convolution SAL technique, and presents results comparing the different methods using a snapshot of the tidal sea surface height. Section 3 describes the model configuration used to test the convolution SAL. Section 4 presents results

comparing tidal errors and computational efficiency using the convolution and spherical harmonics approaches. Conclusions are presented in Section 5.

2 Methods and Implementation

The Modular Ocean Model version 6 (MOM6) is a widely used open source numerical ocean general circulation model (Adcroft et al., 2019). The model is hydrostatic and solves either a Boussinesq or non-Boussinesq equation set. Here we use a single layer configuration in which the dynamical equations reduce to the shallow water equations on a sphere,

$$\frac{\partial \boldsymbol{u}}{\partial t} + (\boldsymbol{u}\cdot\nabla)\boldsymbol{u} + \boldsymbol{f}\times\boldsymbol{u} = -g\nabla\eta + \mathcal{F}, \tag{1}$$

$$\frac{\partial \eta}{\partial t} + \nabla\cdot(h\boldsymbol{u}) = 0, \tag{2}$$

where t is time, $\boldsymbol{u}$ is the horizontal fluid velocity, $\boldsymbol{f} = f\boldsymbol{e}_r$, where f is the Coriolis parameter and $\boldsymbol{e}_r$ is the radial outward unit vector, η is the perturbation sea surface height, g is acceleration due to gravity, $\mathcal{F}$ are other forces (for instance, friction), and h is the total water column thickness. If the ocean floor has height $b(\boldsymbol{x})$, then $\eta(t,\boldsymbol{x}) = h(t,\boldsymbol{x}) + b(\boldsymbol{x})$. Equation 1 expresses the balance of momentum, and Eq. 2 expresses the conservation of mass. For multi-layer configurations, this system can be supplemented with thermodynamic equations, and in that case it is often replaced by the more general Boussinesq or non-Boussinesq equations. The horizontal grid is based on a global tripolar discretization with an Arakawa C-grid. In this work the forcing term has several components,

$$\mathcal{F} = g\nabla(\eta_{\mathrm{EQ}} + \eta_{\mathrm{SAL}}) + \boldsymbol{F}_{\mathrm{wave}} + \boldsymbol{F}_{\mathrm{quad}} + \boldsymbol{F}_h, \tag{3}$$

where η_{EQ} represents equilibrium tidal forcing, η_{SAL} is the SAL potential, $\boldsymbol{F}_{\mathrm{wave}}$ is the linear wave drag, $\boldsymbol{F}_{\mathrm{quad}}$ is quadratic bottom boundary layer drag, and $\boldsymbol{F}_h$ is horizontal viscosity. The linear wave drag includes a tunable parameter χ. Further details on the wave drag scheme are given by Jayne and St. Laurent (2001) and Buijsman et al. (2015). We refer to η_{SAL} as the SAL potential and $g\nabla\eta_{\mathrm{SAL}}$ as the SAL acceleration.

2.1 Spherical Harmonics for Computing SAL

Recent efforts to compute SAL inline (Barton et al., 2022; Brus et al., 2023; Wang et al., 2024) have used spherical harmonics. In this technique, the spherical harmonics decomposition of the sea surface height η is computed, with spherical harmonic coefficients $\widehat{\eta}_{n,m}$ given by

$$\widehat{\eta}_{n,m} = \int_0^{2\pi}\int_0^{\pi} Y_n^m(\theta,\phi)\eta(\theta,\phi)\cos\theta d\theta d\phi, \tag{4}$$

where Y_n^m is the degree n order m spherical harmonic, θ is the latitude, and ϕ is the longitude. In practice two approaches are available to compute these coefficients. One approach uses a fast spherical harmonics transform (SHT) to reduce the operation count (Barton et al., 2022), but this approach faces challenges with parallel scaling, and additional interpolation steps are

needed if the sea surface height is not given on a latitude-longitude grid. Another approach computes the integrals in Eq. (4) directly without using a fast transform as in Brus et al. (2023) and Wang et al. (2024). In this case the operation count is not reduced, but the direct calculation is better suited for parallelization.

Given the coefficients $\widehat{\eta}_{n,m}$, the SAL potential has the expansion

$$\eta_{\mathrm{SAL}}(\theta,\phi) = \sum_{n=0}^{\infty}\sum_{m=-n}^{n} \frac{3\rho_w(1+k'_n-h'_n)}{\rho_e(2n+1)}\widehat{\eta}_{n,m}Y_n^m(\theta,\phi), \tag{5}$$

where ρ_w and ρ_e are the average density of seawater and the Earth in kilograms per cubic meter, and k'_n and h'_n are the modified load Love numbers (LLNs) as discussed by Farrell (1972). We use average values for the real Earth, $\rho_w = 1035\,\mathrm{kg\,m^{-3}}$, $\rho_e = 5517\,\mathrm{kg\,m^{-3}}$. When a multi-layer model is used, the sea surface height is replaced with the bottom pressure anomaly and the coefficients $\widehat{\eta}_{n,m}$ are adjusted appropriately. In practice the sum in Eq. (5) is truncated, for example going up to degree $N = 40$ (Brus et al., 2023), since using larger degrees has not significantly reduced the tidal error. The fact that tidal errors do not decrease past $N = 40$ can be attributed to Gibbs phenomenon and aliasing errors that occur when high wavenumber components in the solution are projected to low wavenumbers if the underlying spatial grid is not sufficiently fine (Sansò, 1990; Jekeli, 1996; Chen et al., 2009). These errors will be largest in coastal regions, and coastal tides have a significant back effect on the open ocean tides (Arbic et al., 2009). After computing the SAL potential η_{SAL}, the SAL acceleration $g\nabla\eta_{\mathrm{SAL}}$ is computed by finite differences, which can lead to additional errors by amplifying high wavenumber errors in η_{SAL}.

2.2 Gibbs Phenomenon

The Gibbs phenomenon occurs when truncating the Fourier series of a periodic function f with a jump discontinuity (Gottlieb and Shu, 1997). If f has a jump discontinuity, then finite truncations of the Fourier series will overshoot and undershoot around the discontinuity. This overshoot has a magnitude of approximately 9%, and this oscillatory error does not diminish as more terms are used, but instead it becomes sharper and more concentrated around the discontinuity. In the context of computing SAL, the Gibbs phenomenon may arise from the finite truncation of a spherical harmonics series. When computing the spherical harmonic coefficients of the sea surface height $\widehat{\eta}_{m,n}$, the data field η is set to zero over land. While physically reasonable, this essentially introduces a jump discontinuity along coastlines, which adversely affects the convergence of the series. The geodesy community has known about issues with Gibbs phenomenon in spherical harmonics calculations and has advocated for an alternative based on convolution with a Green's function (Merriam, 1980; Schrama, 2005). Before examining that approach however, we consider a method for eliminating the Gibbs phenomenon.

2.3 Cesàro Summation

Cesàro summation is a general method for improving the convergence properties of a series. In the case of the spherical harmonics series in Eq. (4), one defines the partial sums

$$S_J = \sum_{n=0}^{J}\sum_{m=-n}^{n} \frac{3\rho_w(1+k'_n-h'_n)}{\rho_e(2n+1)}\widehat{\eta}_{n,m}Y_n^m(\theta,\phi), \tag{6}$$

and then averages them to obtain the approximation

$$\eta_{\mathrm{SAL}}(\theta,\phi) \approx \frac{1}{N+1}\sum_{J=0}^{N} S_J, \tag{7}$$

which is equivalent to modifying the coefficients of the original series,

$$\eta_{\mathrm{SAL}}(\theta,\phi) \approx \sum_{n=0}^{N}\sum_{m=-n}^{n}\left(1-\frac{n}{N+1}\right)\frac{3\rho_w(1+k'_n-h'_n)}{\rho_e(2n+1)}\widehat{\eta}_{n,m}Y_n^m(\theta,\phi). \tag{8}$$

This technique can be implemented by modifying the existing spherical harmonics computation with no additional cost. The hope is that this technique will reduce the Gibbs phenomenon along coastlines, however at the same time, it introduces an error by effectively modifying the LLNs. As far as we know, Cesàro summation has not previously been applied in spherical harmonics SAL computations.

2.4 Convolution for Computing SAL

It is well known that the SAL potential can be computed as a convolution on the unit sphere S,

$$\eta_{\mathrm{SAL}}(\boldsymbol{x}) = \int_S G_{\mathrm{SAL}}(\boldsymbol{x}\cdot\boldsymbol{y})\eta(\boldsymbol{y})dS(\boldsymbol{y}), \quad \boldsymbol{x},\boldsymbol{y}\in S, \tag{9}$$

where the SAL Green's function is

$$G_{\mathrm{SAL}}(\boldsymbol{x},\boldsymbol{y}) = \sum_{n=0}^{\infty}\frac{3\rho_w(1+k'_n-h'_n)}{4\pi\rho_e}P_n(\boldsymbol{x}\cdot\boldsymbol{y}), \tag{10}$$

and P_n is the n-th degree Legendre polynomial (Farrell, 1972, 1973). Given a set of grid cells covering the sphere, the integral in Eq. (9) is computed using a numerical quadrature scheme. However, truncating the Legendre series in Eq. (10) and evaluating the result at a large number of grid points is computationally intensive and not feasible in an ocean model where the SAL term is computed inline at every time step. Previous investigators have employed approximations for the LLNs (Farrell, 1972; Guo et al., 2004; Schrama, 2005; Martens et al., 2019) outside the context of an ocean model and focusing primarily on processing data. Because of the limitations of an ocean model, we take an alternative approach to maintain a reasonable runtime. Working with the LLNs in Wang et al. (2012), we empirically determined the following approximations,

$$k'_n \approx a_1/n, \quad h'_n \approx b_0 + b_1/n, \quad a_1 = -2.7, \quad b_0 = -6.21196, \quad b_1 = 6.1. \tag{11}$$

Then substituting in Eq. (10) and using the identities (Gradshteyn and Ryzhik, 2014),

$$\sum_{n=0}^{\infty}P_n(x) = \frac{1}{\sqrt{2(1-x)}}, \quad \sum_{n=1}^{\infty}\frac{1}{n}P_n(x) = -\ln\left(\sqrt{\frac{1-x}{2}}+\frac{1-x}{2}\right), \tag{12}$$

a closed form approximation for the Green's function is obtained,

$$G_{\mathrm{SAL}}(\boldsymbol{x},\boldsymbol{y}) \approx \frac{3\rho_w}{4\pi\rho_e}\left(\frac{1-b_0}{\sqrt{2-2\boldsymbol{x}\cdot\boldsymbol{y}}} - (a_1-b_1)\ln\left(\sqrt{\frac{1-\boldsymbol{x}\cdot\boldsymbol{y}}{2}}+\frac{1-\boldsymbol{x}\cdot\boldsymbol{y}}{2}\right)\right). \tag{13}$$

From Eq. (3) we see that what is needed is the gradient of the SAL potential, $\nabla\eta_{\mathrm{SAL}}$. Assuming η_{SAL} has been computed, the gradient could be obtained by finite differences, but this could lead to large errors in coastal regions. Instead, taking the gradient of Eq. (9), one obtains

$$\nabla\eta_{\mathrm{SAL}}(\boldsymbol{x}) = \int_S \nabla G_{\mathrm{SAL}}(\boldsymbol{x}\cdot\boldsymbol{y})\eta(\boldsymbol{y})dS(\boldsymbol{y}), \tag{14}$$

where the gradient falls on the $\boldsymbol{x}$-variable of the Green's function. The chain rule yields the gradient of the Green's function,

$$\nabla G_{\mathrm{SAL}}(\boldsymbol{x}\cdot\boldsymbol{y}) = \frac{dG_{\mathrm{SAL}}(\cos\gamma)}{d\cos\gamma}\nabla\cos\gamma(\boldsymbol{x},\boldsymbol{y}), \tag{15}$$

where $\boldsymbol{x}\cdot\boldsymbol{y} = \cos\gamma(\boldsymbol{x},\boldsymbol{y})$ and $\gamma(\boldsymbol{x},\boldsymbol{y})$ is the great circle angle between $\boldsymbol{x}$ and $\boldsymbol{y}$. Then taking these derivatives yields

$$\nabla G_{\mathrm{SAL}}(\boldsymbol{x},\boldsymbol{y}) = \frac{3\rho_w}{4\pi\rho_e R_E\sqrt{1-x_3^2}}\begin{bmatrix} y_3(1-x_3^2) - x_3(x_1y_1+x_2y_2) \\ x_1y_2 - x_2y_1 \end{bmatrix}\left(\frac{1-b_0}{(2-2\boldsymbol{x}\cdot\boldsymbol{y})^{3/2}} - \frac{(a_1-b_1)(2\boldsymbol{x}\cdot\boldsymbol{y}+\sqrt{2-2\boldsymbol{x}\cdot\boldsymbol{y}})}{2((\boldsymbol{x}\cdot\boldsymbol{y})^2-1)}\right), \tag{16}$$

where (x_1,x_2,x_3) and (y_1,y_2,y_3) are the Cartesian coordinates of $\boldsymbol{x}$ and $\boldsymbol{y}$. Previous approaches based on Kummer's transformation yield approximate Green's functions similar to Eq. (13), but with an additional Legendre series to correct for the low wavenumber behavior. While this is computationally feasible in an offline context, summing a Legendre series up to $N = 10$ increases the runtime for evaluating the Green's function by a factor of 3, and going to $N = 40$ increases the runtime by a factor of 18. Hence we choose to work with the closed form approximate Green's function in Eq. (13) as a reasonable compromise between accuracy and efficiency for inline SAL calculations.

2.5 Fast Summation for Accelerating Convolutions

We employ a midpoint discretization of Eq. (14) yielding an approximation for the gradient of the SAL potential,

$$\nabla\eta_{\mathrm{SAL}}(\boldsymbol{x}_i) \approx \sum_{j=1,j\neq i}^{N_0} \nabla G_{\mathrm{SAL}}(\boldsymbol{x}_i,\boldsymbol{x}_j)\eta(\boldsymbol{x}_j)A_j, \quad i = 1,\ldots,N_0, \tag{17}$$

where N_0 is the number of grid cells used in MOM6, $\boldsymbol{x}_i$ is the midpoint of a grid cell, and A_i is the grid cell area. As the SAL acceleration is computed at cell centers, interpolation is performed to obtain values at cell edges. The kernel singularity at $i = j$ is skipped, which is consistent with taking the Cauchy principal value of the integral. If the sums in Eq. (17) are computed directly using loops over the indices i and j, the operation count scales like $O(N_0^2)$, which is prohibitive for reaching high resolution. Various fast summation methods have been developed to accelerate the computation of such sums including the treecode (Barnes and Hut, 1986) and Fast Multipole Method (Greengard and Rokhlin, 1987).

Here we employ the recently developed Cubed Sphere Fast Multipole Method (CSFMM) to reduce the operation count to $O(N_0)$ (Chen and Krasny, 2025). The CSFMM applies barycentric Lagrange interpolation to approximate the kernel (Berrut and Trefethen, 2004), with proxy points defined by a tensor product grid of Chebyshev points in a quadtree of cubed sphere

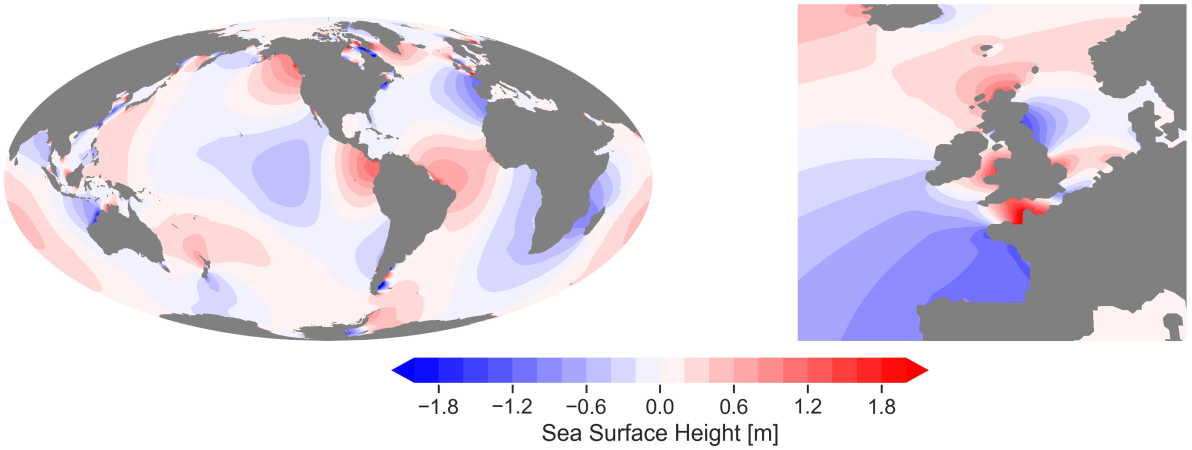

Figure 1. Global snapshot of tidal sea surface height used to compare different SAL computation methods. The right panel is a zoomed version of the left panel focusing on the Northeast Atlantic, a region of exceptionally large coastal tides. The SSH snapshot is on a MOM6 grid with 0.08° nominal grid spacing, taken from an existing MOM6 barotropic tidal simulation.

grid cells. The scheme introduces an error whose amplitude is controlled by two user-specified parameters, the interpolation degree n_0 and a parameter θ_0 controlling the size and separation of the cubed sphere grid cells. In contrast to spherical harmonics approximations, the interpolation is local, and this approach does not encounter the Gibbs phenomenon. In addition, the quadtree structure of the cubed sphere grid cells naturally adapts to the irregular distribution of ocean grid points around coastlines. A detailed discussion of the error behavior of spherical convolutions and the CSFMM is presented in Chen and Krasny (2025).

2.6 Comparison of Methods

Before discussing the implementation of convolution SAL in MOM6, we compare the various methods for computing SAL without any confounding factors the model may introduce. We compute the SAL acceleration on a MOM6 grid with 0.08° nominal grid spacing for the global snapshot of tidal sea surface height (SSH) shown in Fig. 1 using the various methods described in the previous sections. The SSH snapshot comes from a tidal MOM6 run, with SAL computed using the SHT with $N = 40$. For future reference, note that the SSH in Fig. 1 apparently has discontinuities along certain coastlines. In the following tests, the SHT is used with maximum degree $N = 40$ and $N = 200$, and the Cesàro SHT is used with $N = 40$, $N = 200$, and $N = 400$. These are compared with the convolution approach, which uses CSFMM parameters $n_0 = 2$ and $\theta_0 = 0.9$. Global zonal and meridional accelerations are plotted in Figs. 2 and 3, and accelerations focused on the Northeast Atlantic are plotted in Figs. 4 and 5. Figure 6 plots the spectral density of the zonal acceleration in Fig. 2. As all the calculations are based on the same reference SSH snapshot, differences can be attributed to the different methods of computing SAL, as opposed to confounding factors from the other (non-SAL) factors in the model, such as wave drag, bathymetry, and so on.

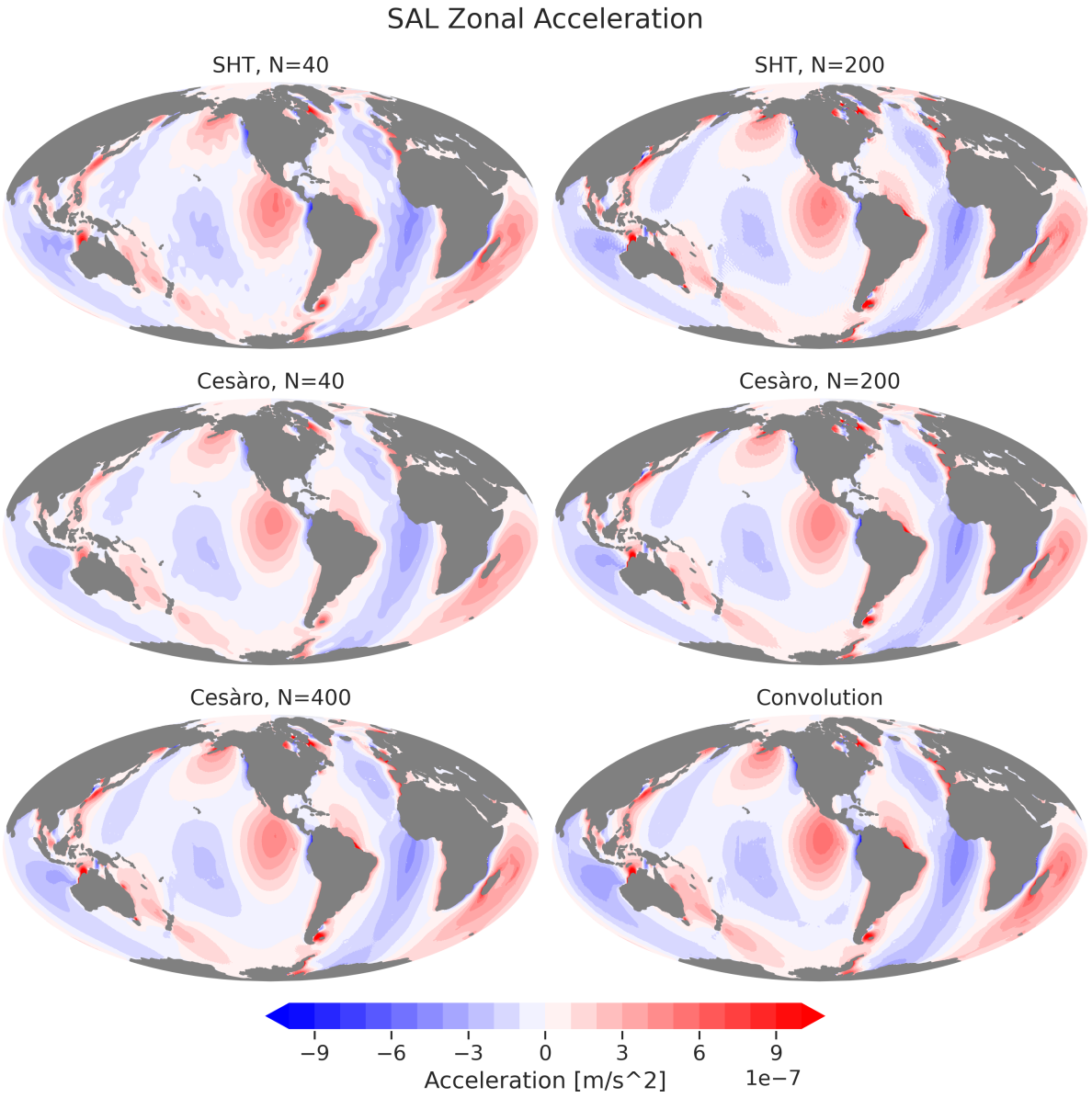

Figure 2. SAL zonal acceleration for the tidal sea surface height snapshot in Fig. 1, computed using spherical harmonics transform (SHT) with $N = 40, N = 200$, Cesàro regularized SHT with $N = 40, N = 200, N = 400$, and convolution.

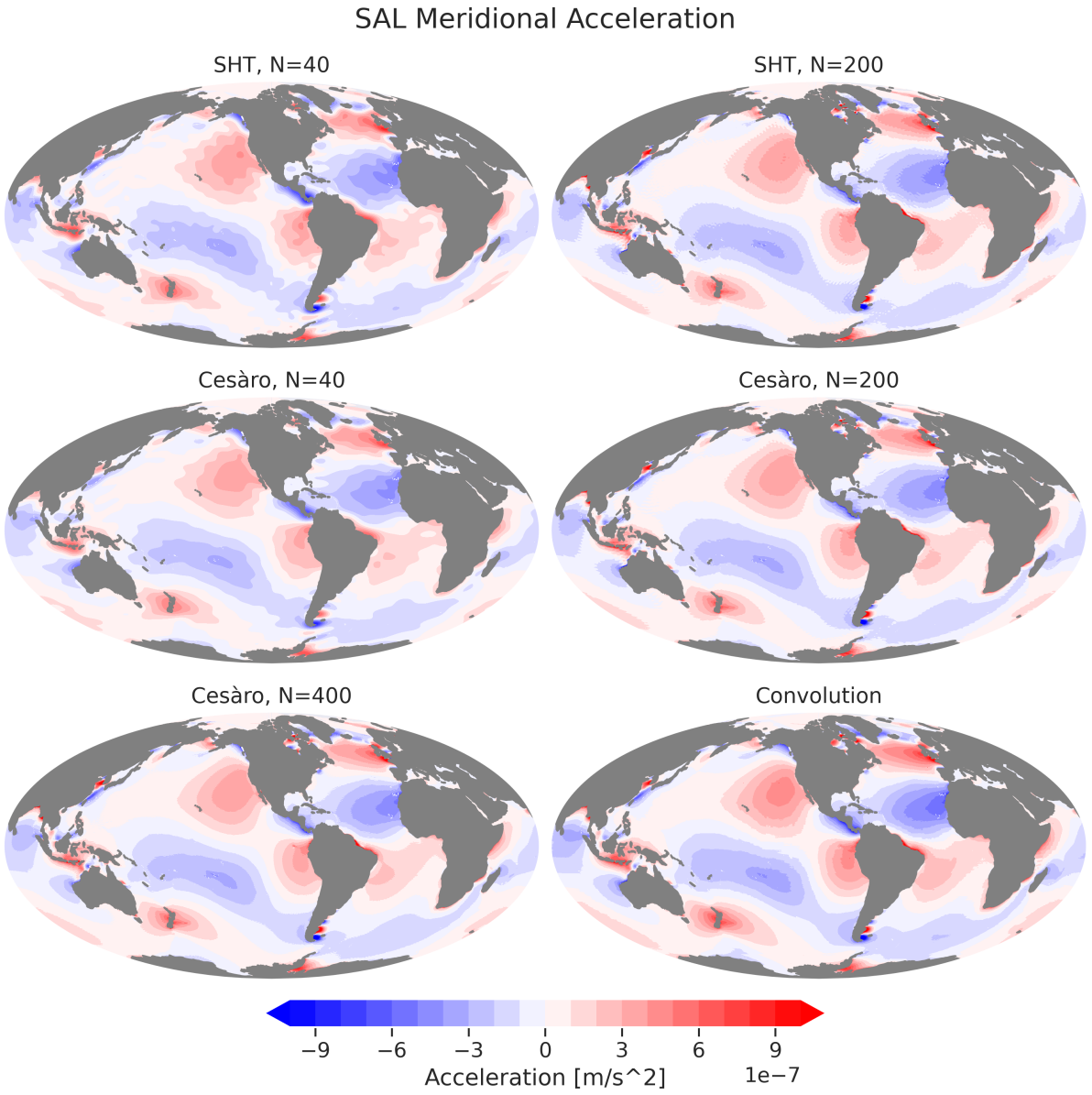

Figure 3. SAL meridional acceleration for the sea surface height snapshot in Fig. 1, computed using spherical harmonics transform (SHT) with $N = 40, N = 200$, Cesàro regularized SHT with $N = 40, N = 200, N = 400$, and convolution.

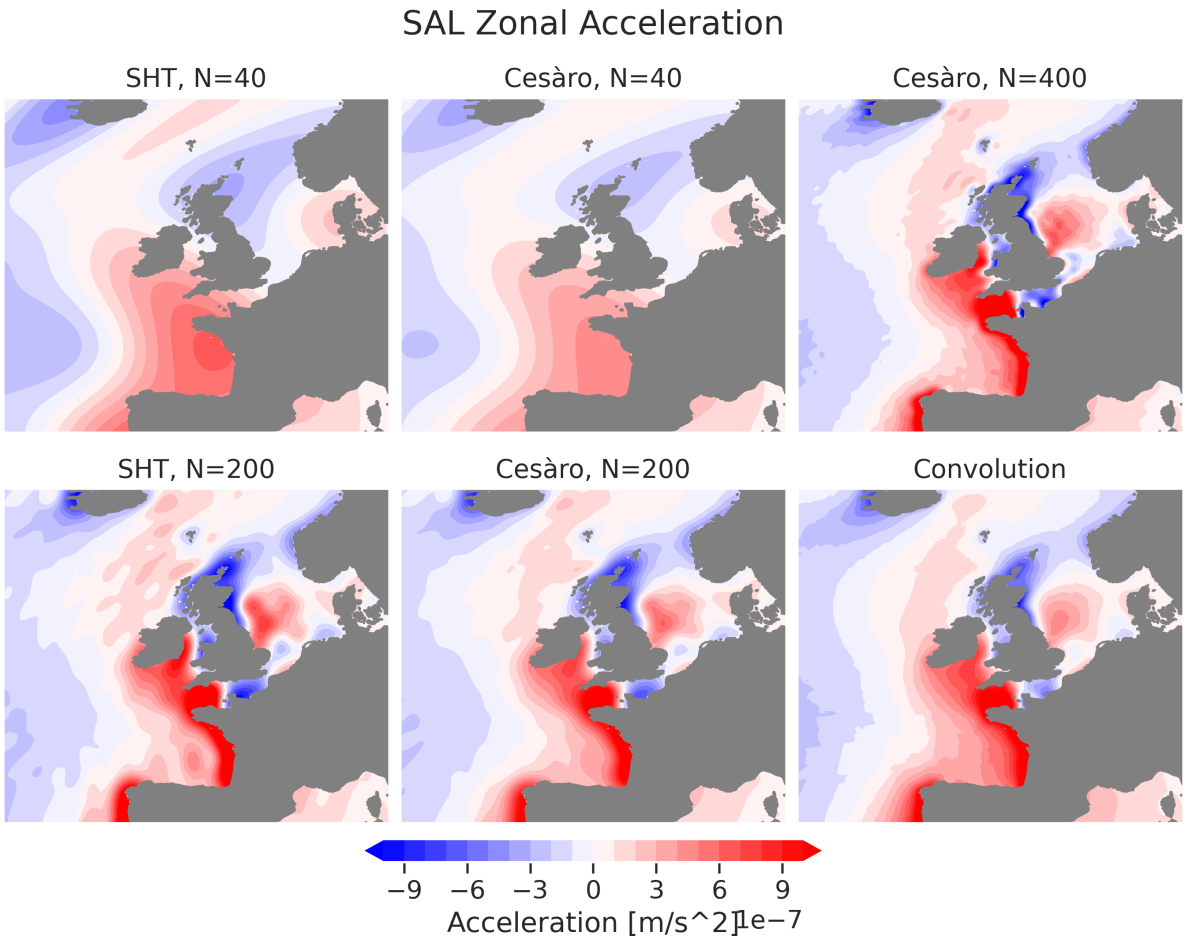

Figure 4. As in Fig. 2, focusing on the Northeast Atlantic.

Looking first at the global zonal and meridional accelerations, there is general agreement among all the results. As the maximum degree increases from $N = 40$ to $N = 200$ in the SHT computation, one observes less large scale waviness in the contour lines, due to a reduction in truncation error. While differences between the $N = 40$ and $N = 200$ results may appear large, they are actually quite small, less than $10^{-8}\mathrm{m\,s}^{-2}$ in the open ocean. Additionally, the large scale patterns of the Cesàro SHT result broadly match the unmodified SHT result, with small differences. This is because Cesàro summation has the largest effect on small scales at high wavenumber, while the plots mainly depict the low wavenumber large scale structure. Lastly, there are some differences in the large scale structure between the convolution result and the five SHT computations. This is because the LLN approximations used in deriving the closed form SAL Green's function are least accurate at low wavenumber and have the greatest impact at large scales.

Next consider the regional accelerations in Figs. 4 and 5. Clear differences can be seen between the SHT results with $N = 40$ and $N = 200$, where $N = 200$ resolves small scale features in coastal regions while predicting larger coastal amplitudes. As

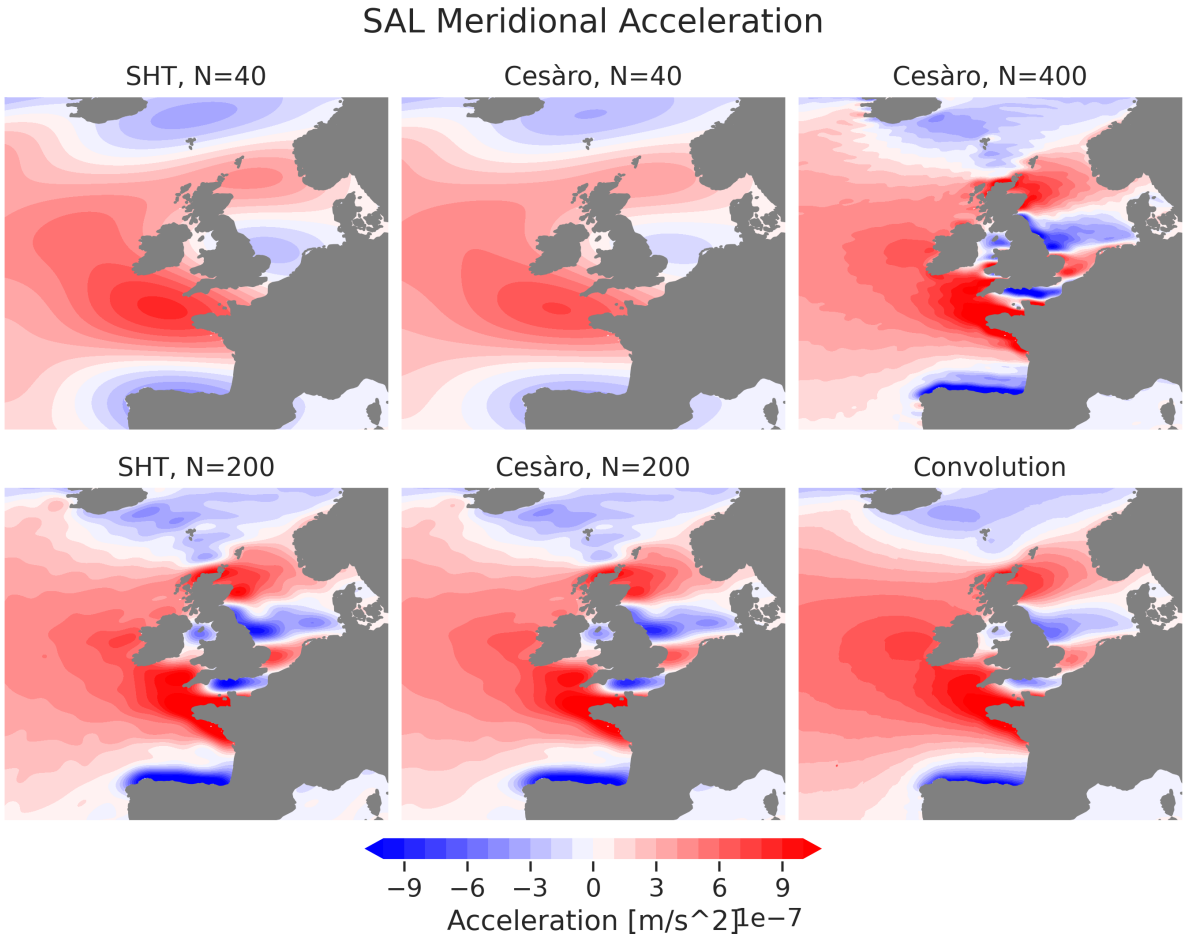

Figure 5. As in Fig. 3, focusing on the Northeast Atlantic.

coastal regions are spanned by relatively few grid cells, aliasing of high degree spherical harmonics may contribute to these large amplitudes. Comparing the $N = 40$ SHT result with the $N = 40$ Cesàro SHT result, one sees the regularization effect of the latter as maximum amplitudes are smaller. At $N = 200$, the Cesàro sum resolves most of the small scale structure of the unmodified SHT, but there is less waviness in the contour lines and the maximum amplitudes are smaller. The $N = 400$ Cesàro result further reduces the waviness and resolves small scale features, but also increases the coastal amplitudes. The convolution result is similar to the high degree SHT results, but it predicts smaller coastal amplitudes. The LLN approximations used in deriving the closed form SAL Green's function are most accurate at high wavenumber and small scales. While the convolution approach has errors in the approximation SAL Green's function, quadrature error in computing the integral, and interpolation error from the CSFMM, it avoids the Gibbs phenomenon, aliasing error, and finite difference errors present in the SHT calculations.

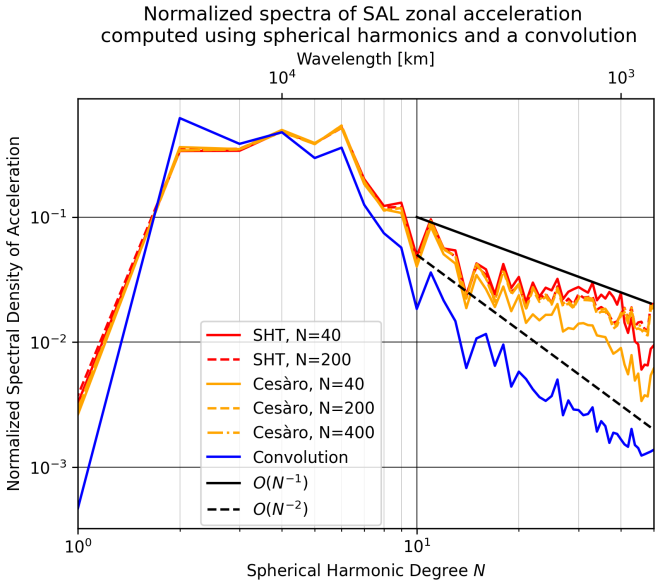

Figure 6. Normalized spectral density of the global SAL zonal acceleration field shown in Fig. 2. A spherical harmonic of degree N has wavelength $2\pi R_E/N$.

To gain further insight into the methods, Fig. 6 shows the normalized spectral density of the SAL zonal acceleration. There is general agreement among the five SHT results, which decay roughly as $O(N^{-1})$. Comparing the $N = 40$ SHT with the $N = 40$ Cesàro SHT, the latter spectrum falls off slightly faster at high wavenumber. A similar trend is seen at $N = 200$, but to a lesser degree. In contrast, the convolution spectrum falls off significantly faster at high wavenumber, decaying like $O(N^{-2})$, which is consistent with the smoother acceleration fields seen in Fig. 4 and Fig. 5.

3 Simulation Details

The convolution/CSFMM technique described above was implemented in MOM6. The model is run with zero initial velocity and M_2 tidal forcing for 20 days with time step $\Delta t = 180\,\mathrm{s}$. The SAL acceleration is computed inline at every time step and the last three days of output are used to evaluate the results. A single level configuration is used with two different grids, one with nominal spacing $0.36°$ (typical of long duration low-resolution climate simulations), and one with nominal spacing $0.08°$ (typical of short duration high-resolution simulations). The model was run on the Derecho computer system at NCAR (Computational and Information Systems Laboratory, 2023). The topography and wave drag are based on GEBCO 2023. Several configurations are tested: SHT with $N = 40, 200$, Cesàro SHT with $N = 40, 200, 400$, and convolution.

3.1 Measuring Error

To measure the error in the model tides, the model output is compared with the TPXO9 dataset (Erofeeva and Egbert, 2018), which comes from a hydrodynamical model that assimilates satellite observations of tidal sea surface heights. We first compute

$$D^2 = \frac{1}{2}(A^2_{\mathrm{TPXO}} - A^2_{\mathrm{MOM6}}) - A_{\mathrm{TPXO}} A_{\mathrm{MOM6}} \cos(\varphi_{\mathrm{TPXO}} - \varphi_{\mathrm{MOM6}}), \tag{18}$$

at each grid point, where A is the amplitude of the tidal constituent and φ is the Greenwich phase lag. The root mean square error (RMSE) is then defined as

$$\mathrm{RMSE} = \left(\frac{1}{4\pi R_E^2} \int_S D^2 dS \right)^{1/2}. \tag{19}$$

The RMSE can be decomposed into an amplitude error and a phase error (Shriver et al., 2012). The RMSE is also computed for two different domains: over the entire ocean, and over grid points lying between 66° south and 66° north that have a depth of greater than 1000 meters. The latter computation removes coastal regions and polar regions, where data-assimilative tide models such as TPXO are less accurate (Stammer et al., 2014).

3.2 Tuning

The parameter χ in the wave drag scheme is tuned for each method of computing SAL in order to minimize the RMSE. One can understand the need for tuning using energy arguments (Arbic et al., 2004); if χ is too large, then too much energy is dissipated, and conversely if χ is too small, then not enough energy is dissipated. Both extremes adversely affect the accuracy of the modeled tides. The different methods of computing SAL yield accelerations of different amplitude and χ must change accordingly. The χ parameters used here are presented in Table 1 and Table 2. Because of differences in how the wave drag was precomputed, the coefficient χ has a different order of magnitude at 0.36° and 0.08° grid spacing.

4 Results

4.1 TPXO9 Comparison

Error results are presented in Table 1 with 0.36° nominal grid spacing and in Table 2 with 0.08° nominal grid spacing. Denoting the maximum degree of spherical harmonics used as N, the SHT is compared with the Cesàro SHT, as well as the convolution. With 0.36° nominal grid spacing, the $N = 40$ SHT has a deep non-polar RMSE of 6.50 cm, with the phase error contributing 5.70 cm. The global RMSE of 8.65 cm is similarly dominated by the phase error of 7.31 cm. Using $N = 200$ yields only an error reduction of approximately 1%. The Cesàro SHT errors decrease from $N = 40$ to $N = 200$ and $N = 400$, yet even for $N = 400$ they remain larger than the $N = 40$ SHT errors. The convolution errors are smaller than the SHT errors in all cases, with the greatest reduction coming from the phase error. With 0.08° nominal grid spacing, significant error reduction is

achieved in all cases. The $N = 200$ SHT errors are the smallest among the five SHT test cases. The amplitude errors are slightly larger for the convolution than for the $N = 200$ SHT, but this is compensated by smaller phase errors, so that the convolution has the smallest RMSE.

4.2 Discussion

The question arises–why are the SHT errors only slightly smaller for $N = 200$ than for $N = 40$? Figure 2 and Fig. 3 show that the $N = 40$ SHT results have small amplitude oscillations in the open ocean, while the $N = 200$ SHT results have similar structure but without the oscillations. The more significant difference is seen in Fig. 4 and Fig. 5, where $N = 200$ yields larger coastal accelerations than $N = 40$. Some of these large coastal accelerations are spurious overshoots due to Gibbs phenomenon, aliasing error, and finite differencing error. Similar considerations apply to the $N = 200$ and $N = 400$ Cesàro SHT results. Cesàro summation mitigates any impact of Gibbs phenomenon, but it does nothing to remedy errors due to aliasing and finite differencing, and as a result, it also results in large coastal accelerations. By contrast as seen in Fig. 4 and Fig. 5, the convolution predicts smaller coastal accelerations, which we attribute to the absence of Gibbs phenomenon, aliasing error, and finite differencing error.

Another question arises–why does the removal of Gibbs phenomenon and aliasing error in coastal regions reduce the error in the deep non-polar ocean? We speculate that the global improvement in the tides is due to the back effect of large resonant coastal tides upon open-ocean tides (Arbic et al., 2007, 2009; Arbic and Garrett, 2010). Thus it appears that improvements to the SAL in coastal regions as a result of using the convolution can drive improvements to the tides in the entire ocean. Further exploration into the role of the back effect in these calculations, as well as other potential reasons for the improvement, is left as a topic for future work.

4.3 Parallel Efficiency and Runtime

A strong scaling analysis is performed to examine the parallel efficiency and runtime of the convolution/CSFMM SAL. Figure 7 shows the single time step runtime (seconds) versus the number of MPI ranks for MOM6 running with 0.36° nominal grid spacing yielding $N_0 = 784000$ grid cells. The runtime is shown for the convolution/CSFMM SAL, $N = 40$ spherical harmonics

		Deep non-polar ocean			Global ocean		
0.36° nominal grid spacing	Wave drag χ	RMSE	Amplitude error	Phase error	RMSE	Amplitude error	Phase error
Spherical harmonic SAL, $N = 40$	0.8	6.50	3.18	5.70	8.65	4.63	7.31
Spherical harmonic SAL, $N = 200$	0.8	6.45	3.09	5.66	8.54	4.61	7.18
Cesàro SH SAL, $N = 40$	0.8	8.10	3.56	7.27	10.26	5.01	8.95
Cesàro SH SAL, $N = 200$	0.8	6.76	3.17	5.98	8.86	4.68	7.52
Cesàro SH SAL, $N = 400$	0.8	6.60	3.13	5.81	8.69	4.65	7.35
Convolution SAL	0.7	4.10	2.78	3.01	6.53	4.43	4.80

Table 1. Wave drag tuning parameter χ and errors for different methods of computing SAL with 0.36° nominal grid spacing.

		Deep non-polar ocean			Global ocean		
0.08° nominal grid spacing	Wave drag χ	RMSE	Amplitude error	Phase error	RMSE	Amplitude error	Phase error
Spherical harmonic SAL, $N = 40$	8.0	2.71	1.59	2.20	5.32	3.54	3.96
Spherical harmonic SAL, $N = 200$	8.0	2.67	1.55	2.17	5.22	3.53	3.84
Cesàro SH SAL, $N = 40$	8.0	4.50	2.34	3.85	6.78	3.98	5.49
Cesàro SH SAL, $N = 200$	8.0	3.01	1.68	2.49	5.48	3.61	4.13
Cesàro SH SAL, $N = 400$	8.0	2.84	1.61	2.33	5.35	3.57	3.98
Convolution SAL	8.2	2.36	1.70	1.63	5.06	3.64	3.52

Table 2. As in Table 1, but with 0.08° nominal grid spacing.

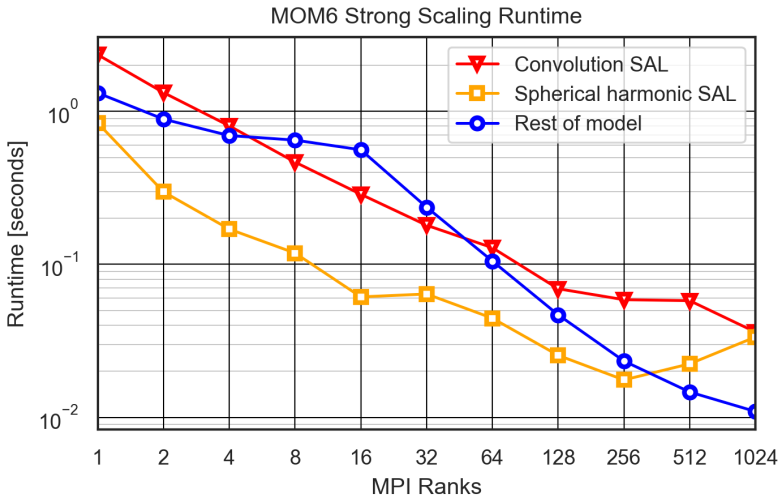

Figure 7. Single time step runtime (seconds) versus number of MPI ranks, MOM6 running with 0.36° nominal grid spacing, yielding $N_0 = 784000$ grid cells, results shown for convolution SAL, $N = 40$ spherical harmonics SAL, non-SAL portion of the calculation.

SAL, and non-SAL portion of the calculation. The data was collected using the internal performance analysis tools in MOM6. The SHT and convolution/CSFMM are different algorithms with different operation counts and communication patterns, and this affects their parallel efficiency. From 1 to 16 ranks, the SHT scales better and is faster than the convolution/CSFMM, but from 16 to 1024 ranks the convolution/CSFMM scales better than the SHT. The SHT runtime increases at 512 and 1024 ranks, presumably due to communication costs, while the convolution/CSFMM continues scaling well. In this single layer simulation the convolution/CSFMM runtime is comparable to or smaller than the non-SAL portion of the calculation, and its impact in a multi-layer simulation will be much smaller.

5 Conclusions

In the numerical modeling of ocean tides, capturing the effects of SAL is necessary for accurate prediction of tidal amplitude and phase. Many current models employ spherical harmonics to compute the SAL acceleration. This work presents an alternative where the SAL acceleration is computed by convolving the sea surface height with an approximate Green's function. The convolution integral is discretized on a set of grid cells covering the sphere and the sums are accelerated by the Cubed Sphere Fast Multipole Method. The convolution/CSFMM was implemented in the MOM6 ocean model and compared with the default SHT as well as a Cesàro modified SHT. Errors in tidal amplitude and phase were tabulated using the TPXO9 tidal atlas as the reference. In these tests the convolution has smaller RMSE than the SHT. The larger SHT error is attributed to overshoots in coastal amplitude due to Gibbs phenomenon, aliasing error due to finite grid resolution, and finite difference error in computing the gradient of the SAL potential. In contrast to the global nature of spherical harmonics, the convolution/CSFMM uses local grid cell approximations which do not exhibit these errors. Parallel scaling results up to 1024 MPI ranks show that the runtime of the convolution/CSFMM is not prohibitive.

This work focused on global ocean models, but incorporating tides and SAL in regional models is also of interest (Irazoqui Apecechea et al., 2017). Spherical harmonics are poorly suited for that case, and in future work we plan to explore the convolution/CSFMM SAL in regional models. We also envision improving the accuracy of the closed form Green's function in Eq. (16) by utilizing more accurate approximations of the load Love numbers (Farrell, 1972; Guo et al., 2004; Schrama, 2005; Martens et al., 2019). Similarly, the present work employed a simple discretization of the convolution integral Eq.(17) and more accurate schemes could be considered (Agnew, 2012). Finally, an integral equation method could bypass the load Love numbers and directly compute the SAL Green's function on a grid given a model of the Earth interior. Such an approach could possibly also incorporate the inhomogeneity of the Earth interior (Pagiatakis, 1990; Scherneck, 1991).

Code and data availability. The current version of MOM6 is available from https://github.com/noaa-gfdl/MOM6 under the GNU Lesser General Public License. The exact version of the model used to produce the results used in this paper is archived on repository under DOI 10.5281/zenodo.18445619 (Chen and Wang, 2026), as are input data and scripts to run the model and produce the plots for all the simulations presented in this paper.

Author contributions. BKA and RK conceptualized the project. AC conducted the formal analysis and investigation. AC and HW produced the software. HW provided datasets. BKA and RK supervised the project. AC visualized the results and prepared the original draft. AC, HW, BKA, and RK assisted in reviewing and editing the manuscript.

Competing interests. The authors declare that they have no conflict of interest.

Acknowledgements. AC was supported by the National Science Foundation Graduate Research Fellowship Program under Grant Number DGE 2241144. Any opinions, findings, and conclusions or recommendations expressed in this material are those of the authors and do not necessarily reflect the views of the National Science Foundation. BKA is grateful for sabbatical support from the Australian National University, especially Callum Shakespeare, Andy Hogg, and Adele Morrison, during the 2024–2025 academic year. BKA acknowledges support from Office of Naval Research grant N00017-22-1-2576. The authors thank Robert Hallberg (National Oceanic and Atmospheric Administration, Geophysical Fluid Dynamics Laboratory) and Alan Wallcraft (Florida State University) for useful discussions. The authors also thank Oliver Jahn (MIT, Program in Atmospheres, Oceans, and Climate) for noticing mistakes in the original statements of Equations 15 and 16, which have since been rectified. The authors additionally thank the reviewers for helpful comments.

References

Accad, Y. and Pekeris, C. L.: Solution of the tidal equations for the M2 and S2 tides in the world oceans from a knowledge of the tidal potential alone, Philos. Trans. R. Soc. London, Ser. A, 290, 235–266, 1978.

Adcroft, A., Anderson, W., Balaji, V., Blanton, C., Bushuk, M., Dufour, C. O., Dunne, J. P., Griffies, S. M., Hallberg, R., Harrison, M. J., et al.: The GFDL global ocean and sea ice model OM4. 0: Model description and simulation features, J. Adv. Model. Earth Syst., 11, 3167–3211, 2019.

Agnew, D. C.: SPOTL: Some programs for ocean-tide loading, 2012.

Arbic, B. K.: Incorporating tides and internal gravity waves within global ocean general circulation models: A review, Prog. Oceanogr., 206, 102 824, 2022.

Arbic, B. K. and Garrett, C.: A coupled oscillator model of shelf and ocean tides, Cont. Shelf Res., 30, 564–574, 2010.

Arbic, B. K., Garner, S. T., Hallberg, R. W., and Simmons, H. L.: The accuracy of surface elevations in forward global barotropic and baroclinic tide models, Deep Sea Res. Part II, 51, 3069–3101, 2004.

Arbic, B. K., St-Laurent, P., Sutherland, G., and Garrett, C.: On the resonance and influence of the tides in Ungava Bay and Hudson Strait, Geophys. Res. Lett., 34, 2007.

Arbic, B. K., Karsten, R. H., and Garrett, C.: On tidal resonance in the global ocean and the back-effect of coastal tides upon open-ocean tides, Atmos. Ocean, 47, 239–266, 2009.

Arbic, B. K., Wallcraft, A. J., and Metzger, E. J.: Concurrent simulation of the eddying general circulation and tides in a global ocean model, Ocean Modell., 32, 175–187, 2010.

Barnes, J. and Hut, P.: A hierarchical O(NlogN) force-calculation algorithm, Nature, 324, 446–449, 1986.

Barton, K. N., Pal, N., Brus, S. R., Petersen, M. R., Arbic, B. K., Engwirda, D., Roberts, A. F., Westerink, J. J., Wirasaet, D., and Schindelegger, M.: Global barotropic tide modeling using inline self-attraction and loading in MPAS-Ocean, J. Adv. Model. Earth Syst., 14, e2022MS003 207, 2022.

Berrut, J.-P. and Trefethen, L. N.: Barycentric Lagrange interpolation, SIAM Review, 46, 501–517, 2004.

Brus, S. R., Barton, K. N., Pal, N., Roberts, A. F., Engwirda, D., Petersen, M. R., Arbic, B. K., Wirasaet, D., Westerink, J. J., and Schindelegger, M.: Scalable self attraction and loading calculations for unstructured ocean tide models, Ocean Modell., 182, 102 160, 2023.

Buijsman, M. C., Arbic, B. K., Green, J., Helber, R. W., Richman, J. G., Shriver, J. F., Timko, P., and Wallcraft, A.: Optimizing internal wave drag in a forward barotropic model with semidiurnal tides, Ocean Modell., 85, 42–55, 2015.

Chen, A. and Krasny, R.: A Cubed Sphere Fast Multipole Method, arXiv preprint arXiv:2508.13550, 2025.

Chen, A. and Wang, H.: Convolution Based Self Attraction and Loading in MOM6, https://doi.org/10.5281/zenodo.18445619, 2026.

Chen, J., Wilson, C., and Seo, K.-W.: S2 tide aliasing in GRACE time-variable gravity solutions, Journal of Geodesy, 83, 679–687, 2009.

Computational and Information Systems Laboratory: Derecho: HPE Cray EX System (University Community Computing), NSF: National Center for Atmospheric Research , Boulder, CO, doi:10.5065/qx9a-pg09, 2023.

Cummins, P. F. and Oey, L.-Y.: Simulation of barotropic and baroclinic tides off northern British Columbia, J. Phys. Oceanogr., 27, 762–781, 1997.

Egbert, G. D., Bennett, A. F., and Foreman, M. G.: TOPEX/POSEIDON tides estimated using a global inverse model, J. Geophys. Res.: Oceans, 99, 24 821–24 852, 1994.

Egbert, G. D., Ray, R. D., and Bills, B. G.: Numerical modeling of the global semidiurnal tide in the present day and in the last glacial maximum, J. Geophys. Res., 109, C03 003, 2004.

Erofeeva, S. and Egbert, G. D.: TPXO9-a new global tidal model in TPXO series, in: American Geophysical Union, Ocean Sciences Meeting, 186, pp. PL34C–186, 2018.

Farrell, W. E.: Deformation of the Earth by surface loads, Rev. Geophys., 10, 761–797, 1972.

Farrell, W. E.: A discussion on the measurement and interpretation of changes of strain in the Earth-Earth tides, ocean tides and tidal loading, Philosophical Transactions of the Royal Society of London. Series A, Mathematical and Physical Sciences, 274, 253–259, 1973.

Gordeev, R., Kagan, B., and Polyakov, E.: The effects of loading and self-attraction on global ocean tides: The model and the results of a numerical experiment, J. Phys. Oceanogr., 7, 161–170, 1977.

Gottlieb, D. and Shu, C.-W.: On the Gibbs phenomenon and its resolution, SIAM Rev., 39, 644–668, 1997.

Gradshteyn, I. S. and Ryzhik, I. M.: Table of integrals, series, and products, Academic press, 2014.

Greengard, L. and Rokhlin, V.: A fast algorithm for particle simulations, J. Comput. Phys., 73, 325–348, 1987.

Guo, J., Li, Y., Huang, Y., Deng, H., Xu, S., and Ning, J.: Green's function of the deformation of the Earth as a result of atmospheric loading, Geophy. J. Int., 159, 53–68, 2004.

Hendershott, M.: The effects of solid Earth deformation on global ocean tides, Geophys. J. Int., 29, 389–402, 1972.

Irazoqui Apecechea, M., Verlaan, M., Zijl, F., Le Coz, C., and Kernkamp, H.: Effects of self-attraction and loading at a regional scale: a test case for the Northwest European Shelf, Ocean Dyn., 67, 729–749, 2017.

Jayne, S. R. and St. Laurent, L. C.: Parameterizing tidal dissipation over rough topography, Geophys. Res. Lett., 28, 811–814, 2001.

Jekeli, C.: Spherical harmonic analysis, aliasing, and filtering, Journal of Geodesy, 70, 214–223, 1996.

Kang, S. K., Foreman, M. G., Lie, H.-J., Lee, J.-H., Cherniawsky, J., and Yum, K.-D.: Two-layer tidal modeling of the Yellow and East China Seas with application to seasonal variability of the M2 tide, J. Geophys. Res.: Oceans, 107, 6–1, 2002.

Le Provost, C., Genco, M., Lyard, F., Vincent, P., and Canceil, P.: Spectroscopy of the world ocean tides from a finite element hydrodynamic model, J. Geophys. Res.: Oceans, 99, 24 777–24 797, 1994.

Martens, H. R., Rivera, L., and Simons, M.: LoadDef: A Python-based toolkit to model elastic deformation caused by surface mass loading on spherically symmetric bodies, Earth and Space Science, 6, 311–323, 2019.

Merriam, J.: The series computation of the gravitational perturbation due to an ocean tide, Physics of the Earth and Planetary Interiors, 23, 81–86, 1980.

Merrifield, M. A., Holloway, P. E., and Johnston, T. S.: The generation of internal tides at the Hawaiian Ridge, Geophys. Res. Lett., 28, 559–562, 2001.

Müller, M., Haak, H., Jungclaus, J. H., Sündermann, J., and Thomas, M.: The effect of ocean tides on a climate model simulation, Ocean Modell., 35, 304–313, 2010.

Munk, W. and Wunsch, C.: Abyssal recipes II: Energetics of tidal and wind mixing, Deep Sea Res. Part I, 45, 1977–2010, 1998.

Pagiatakis, S. D.: The response of a realistic Earth to ocean tide loading, Geophys. J. Int., 103, 541–560, 1990.

Parke, M. E. and Hendershott, M. C.: M2, S2, K1 models of the global ocean tide on an elastic Earth, Mar. Geod., 3, 379–408, 1980.

Ray, R. D.: Global ocean tide models on the eve of TOPEX/POSEIDON, IEEE Trans. Geosci. Remote Sens., 31, 355–364, 1993.

Ray, R. D.: Ocean self-attraction and loading in numerical tidal models, Mar. Geod., 21, 181–192, 1998.

Rocha, C. B., Chereskin, T. K., Gille, S. T., and Menemenlis, D.: Mesoscale to submesoscale wavenumber spectra in Drake Passage, Journal of Physical Oceanography, 46, 601–620, 2016.

Sansò, F.: On the aliasing problem in the spherical harmonic analysis, Bulletin géodésique (1976-1995), 64, 313–330, 1990.

Scherneck, H.-G.: A parametrized solid Earth tide model and ocean tide loading effects for global geodetic baseline measurements, Geophys. J. Int., 106, 677–694, 1991.

Schiller, A. and Fiedler, R.: Explicit tidal forcing in an ocean general circulation model, Geophys. Res. Lett., 34, 2007.

Schrama, E. J. O.: Three algorithms for the computation of tidal loading and their numerical accuracy, Journal of Geodesy, 78, 707–714, 2005.

Schwiderski, E.: Global Ocean Tides: The semidiural principal lunar tide (M2), atlas of tidal charts and maps, Naval Surface Weapons Center, 1979.

Shriver, J., Arbic, B. K., Richman, J., Ray, R. D., Metzger, E., Wallcraft, A., and Timko, P.: An evaluation of the barotropic and internal tides in a high-resolution global ocean circulation model, Journal of Geophysical Research: Oceans, 117, 2012.

Shum, C., Woodworth, P., Andersen, O., Egbert, G. D., Francis, O., King, C., Klosko, S., Le Provost, C., Li, X., Molines, J.-M., et al.: Accuracy assessment of recent ocean tide models, J. Geophys. Res.: Oceans, 102, 25 173–25 194, 1997.

Simpson, J. H. and Hunter, J.: Fronts in the Irish sea, Nature, 250, 404–406, 1974.

Stammer, D., Ray, R. D., Andersen, O. B., Arbic, B. K., Bosch, W., Carrere, L., Cheng, Y., Chinn, D. S., Dushaw, B. D., Egbert, G. D., et al.: Accuracy assessment of global barotropic ocean tide models, Rev. Geophys., 52, 243–282, 2014.

Stepanov, V. N. and Hughes, C. W.: Parameterization of ocean self-attraction and loading in numerical models of the ocean circulation, J. Geophys. Res.: Oceans, 109, 2004.

Thomas, M., Sündermann, J., and Maier-Reimer, E.: Consideration of ocean tides in an OGCM and impacts on subseasonal to decadal polar motion excitation, Geophys. Res. Lett., 28, 2457–2460, 2001.

Wang, H., Xiang, L., Jia, L., Jiang, L., Wang, Z., Hu, B., and Gao, P.: Load Love numbers and Green's functions for elastic Earth models PREM, iasp91, ak135, and modified models with refined crustal structure from Crust 2.0, Comput. Geosci., 49, 190–199, 2012.

Wang, H., Hallberg, R., Wallcraft, A. J., Arbic, B. K., and Chassignet, E. P.: Improving global barotropic tides with sub-grid scale topography, J. Adv. Model. Earth Syst., 16, e2023MS004 056, 2024.

Waterhouse, A. F., MacKinnon, J. A., Nash, J. D., Alford, M. H., Kunze, E., Simmons, H. L., Polzin, K. L., St. Laurent, L. C., Sun, O. M., Pinkel, R., et al.: Global patterns of diapycnal mixing from measurements of the turbulent dissipation rate, J. Phys. Oceanogr., 44, 1854–1872, 2014.